

Did Kepler-444 have a long-lived convective core?

Mark Lykke Winther^{1*}, Víctor Aguirre Børsen-Koch^{2†}, Jakob Lysgaard Rørsted^{1‡},
Amalie Stokholm^{3,4,1}, and Kuldeep Verma^{5,1}.

¹*Stellar Astrophysics Centre, Department of Physics and Astronomy, Aarhus University, Ny Munkegade 120, DK-8000 Aarhus C, Denmark*

²*DARK, Niels Bohr Institute, University of Copenhagen, Jagtvej 128, 2200 Copenhagen, Denmark*

³*Dipartimento di Fisica e Astronomia, Università degli Studi di Bologna, Via Gobetti 93/2, I-40129 Bologna, Italy*

⁴*INAF – Osservatorio di Astrofisica e Scienza dello Spazio di Bologna, Via Gobetti 93/3, I-40129 Bologna, Italy*

⁵*Department of Physics, Indian Institute of Technology (BHU), Varanasi-221005, India*

Accepted XXX. Received YYY; in original form ZZZ

ABSTRACT

With the greater power to infer the state of stellar interiors provided by asteroseismology, it has become possible to study the survival of initially convective cores within stars during their main-sequence evolution. Standard theories of stellar evolution predict that convective cores in sub-solar mass stars have lifetimes below 1 Gyr. However, a recent asteroseismic study of the star Kepler-444 concluded that the initial convective core had survived for nearly 8 Gyr. The goal of this paper is to study the convective-core evolution of Kepler-444 and to investigate its proposed longevity. We modify the input physics of stellar models to induce longer convective-core lifetimes and vary the associated parameter across a dense grid of evolutionary tracks. The observations of metallicity, effective temperature, mean density, and asteroseismic frequency ratios are fitted to the models using the BASTA pipeline. We explore different choices of constraints, from which a long convective-core lifetime is only recovered for a few specific combinations: mainly from the inclusion of potentially unreliable frequencies and/or excluding the covariances between the frequency ratios; while for the classical parameters, the derived luminosity has the largest influence. For all choices of observables, our analysis reliably constrains the convective-core lifetime of Kepler-444 to be short, with a median around 0.6 Gyr and a 1σ upper bound around 3.5 Gyr.

Key words: asteroseismology – convection – stars: evolution – stars: interiors – stars: oscillations – stars: low-mass

1 INTRODUCTION

Understanding and accurately modelling stars is essential to understanding the formation and evolution of the Universe. For instance, accurate determinations of stellar ages and chemical abundances, which are necessary for that, rely on matching observations to theoretical models. While only the surface of stars can be observed, the interior structure and evolution have a major influence on the fundamental stellar parameters such as its age. However, thanks to the CoRoT, *Kepler*, and TESS missions (Baglin et al. 2006; Borucki et al. 2010; Howell et al. 2014; Ricker et al. 2014), it is now possible to measure the intrinsic global oscillations in solar-like stars. The study of these is called *asteroseismology* and it concerns how these oscillations can be used to prescribe and constrain the internal structure of the stars (e.g. Chaplin & Miglio 2013). As these oscillations probe different depths into the stellar interior, these make it possible to better study stellar structure and interior processes. This is especially important in the study of convection within stars as it is currently one of the least understood phenomena that simultaneously has a large impact on the evolution (see i.e. Nordlund et al. 2009; Trampedach 2010; Salaris & Cassisi 2017). Asteroseismology pro-

vides the means to study and constrain the appearance of convective zones in stellar interiors and thus allows us to adjust and improve our stellar models to provide more accurate descriptions of stars.

A variety of asteroseismic quantities can be determined depending on the quality of observations. The two most readily available are the mean large frequency separation, $\Delta\nu$, and the frequency of maximum power, ν_{\max} , that can be used to match observations to models like classical parameters of stars such as the effective temperature and metallicity. Given a higher quality of the data, the individual frequencies can be determined. These are denoted by $\nu_{n,\ell}$, where n is the radial order and ℓ the spherical degree. The observed individual frequencies provide better constraints when comparing them to the corresponding model frequencies, however such comparisons are subject to the problem of the so-called asteroseismic surface effect (Brown 1984; Christensen-Dalsgaard & Gough 1984; Christensen-Dalsgaard et al. 1988). This problem is the result of a model effect, where a simple parametrisation of highly turbulent convection using mixing-length theory leads to substantial errors in the predicted stratification of the outermost layers and hence in the calculated adiabatic oscillation frequencies. Furthermore, it is also caused by the non-adiabatic effects and the uncertainty in our understanding of the convection-oscillation interactions which makes the model frequencies uncertain. This overall causes there to be a deviation between model and observed frequencies, increasing with higher frequencies. It is therefore necessary to account for this by applying an ad-hoc

* E-mail: mark@phys.au.dk

† Formerly Víctor Silva Aguirre

‡ Formerly Jakob Rørsted Mosumgaard

surface correction (Kjeldsen et al. 2008; Ball & Gizon 2014; Sonoi et al. 2015), which relies on additional parameters, when comparing individual frequencies.

A second option is to circumvent the surface effect by instead using the *frequency separation ratios*, or simply called the frequency ratios. Proposed by Roxburgh & Vorontsov (2003, 2013), these are constructed to be independent of the surface effect and instead be sensitive to the interior structure/convective zones of the star. This allows for the determination of e.g. convective core size and convective overshoot (Silva Aguirre et al. 2011, 2013; Deheuvels et al. 2016; Zhang et al. 2022). The frequency ratios are constructed as

$$\begin{aligned} r_{01}(n) &= \frac{d_{01}(n)}{\Delta\nu_1(n)}, \\ r_{02}(n) &= \frac{d_{0,2}(n)}{\Delta\nu_1(n)}, \end{aligned} \quad (1)$$

with the individual large frequency separations defined as $\Delta\nu_l(n) = \nu_{n,l} - \nu_{n-1,l}$. The five-point small frequency separations are given as

$$d_{01}(n) = \frac{1}{8} (\nu_{n-1,0} - 4\nu_{n-1,1} + 6\nu_{n,0} - 4\nu_{n,1} + \nu_{n+1,0}), \quad (2)$$

and the small frequency separation

$$d_{0,2}(n) = \nu_{n,0} - \nu_{n-1,2}. \quad (3)$$

An alternative formulation of the ratios is prescribed using the three-point small frequency separation

$$d_{01}^* = 2\nu_{n,0} - (\nu_{n-1,1} + \nu_{n,1}) / 2, \quad (4)$$

which is less correlated than the five-point separation but also less smooth (Roxburgh 2009). The five-point definition is used throughout this work unless otherwise stated. Similar prescriptions can be used to determined the $r_{10}(n)$ ratios, but as it is constructed from the same frequencies as $r_{01}(n)$, using both would lead to overfitting of the data (Roxburgh 2018) and thus $r_{10}(n)$ is not used in this work. Instead, the ratio sequences $r_{01} = \{r_{01}(n), r_{01}(n+1), \dots\}$ and $r_{02} = \{r_{02}(n), r_{02}(n+1), \dots\}$ can be combined into the r_{012} ratio sequence and used in the fitting scheme to match observations to models (as e.g. Verma et al. 2022).

Kepler-444 (also known as KIC 6278762, HIP 94931, and KOI-3158) is one such star with observations of adequate quality to extract individual frequencies. As it is a bright star, it has traditionally been in many studies and surveys (Roman 1955; Eggen 1956; Wilson 1962; Nordström et al. 2004; van Leeuwen 2007). Additionally, since the first transit-like signals exoplanets were detected (Tenenbaum et al. 2013), its compact system of five exoplanets have been extensively studied (Akeson et al. 2013; Campante et al. 2015; Dupuy et al. 2016; Bourrier et al. 2017; Pezzotti et al. 2021; Stalport et al. 2022). More recently, the star itself has been the subject of several asteroseismic studies, partly also to improve the determination of the exoplanet properties. Campante et al. (2015) used observations from *Kepler* to validate its 5 exoplanets through transit analysis. They derived $\Delta\nu$ and ν_{\max} from the observations and used them alongside classical parameters determined from spectroscopy to deduce the fundamental stellar properties of the star using various pipelines. Silva Aguirre et al. (2015) were able to use individual oscillation frequencies of an ensemble of *Kepler* stars including Kepler-444, to determine fundamental stellar properties using a Bayesian scheme. Both studies determined the star to be an old ($\sim 11 \pm 1$ Gyr) sub-solar mass ($\sim 0.748 \pm 0.044 M_{\odot}$) star.

A recent study by Buldgen et al. (2019, hereafter B19) re-analysed the star and found the same fundamental parameters. They also investigated the evolution of its convective core, which was not previously

determined in the other studies. From detailed forward modelling using the observed frequency ratios, it was determined that the star had a large convective core during the first ~ 7.85 Gyr of its evolution. Sub-solar mass stars like Kepler-444 are born fully convective, but quickly retracts to only having a convective core when they reach the zero-age main-sequence. From standard evolution theory we expect the core to become radiative on short evolutionary time scales due to insufficient energy production, as energy is produced via the PP-chain, whereas super-solar mass stars produce energy via the more efficient CNO-cycle (Kippenhahn & Weigert 1990; Kippenhahn et al. 2012). The long-lived convective core from B19 therefore seems to contradict this. The long lifetime of the convective core in their model was produced by including convective overshoot which feeds the existing convective core material from the surrounding layers. This causes an increased energy production and thus requires energy to be transferred via convection for a longer part of its lifetime. Their analysis is elaborated further upon in Section 2.2.

This provides a unique problem to be studied. The question is not whether Kepler-444 currently has a convective core as this is easily extracted from the frequency ratios to not be the case (Silva Aguirre et al. 2011). It is instead a question of whether the frequency ratios provide constraints on the lifetime of the initial convective core when it has long since then contracted and turned radiative. As the frequency ratios are a product of the current internal structure of a star, they will only contain signatures of a disappeared convective core if it is reflected in the internal structure. This signature would be caused by the difference in speed of which the convective core will retract, comparing to a short lifetime convective core model. This causes the composition gradient in the core to be essentially erased for an extended amount of time, thus affecting the sound speed gradient from which the frequency ratios are derived. While this can easily be modelled, the question remains whether this signature is strong enough to alter the frequency ratios significantly.

This work will focus on studying the survival of the birth convective core. Mainly, the lifetime of the convective core will be inferred from fitting the observed parameters of Kepler-444 to a grid of stellar evolutionary tracks with high resolution sampling of convective core extent and lifetimes. The stellar models that best reproduce the observed constraints will then be compared to the results of B19 to investigate the origin of the inferred convective-core lifetime. Additionally, the fit of frequency ratios to the models of B19 will be reanalysed to determine which signatures/contributions lead to their conclusion of a long lifetime convective core being the best fit.

The paper is structured as follows. The observations of Kepler-444 and previous modelling of the star serving as a basis for this paper is presented in Section 2. The method for modelling the star is outlined in Section 3, while the results from fitting the observations to these models are presented in Section 4. The results will be discussed and compared to those of B19 in Section 5, and the conclusion will be presented in Section 6.

2 PREVIOUS STUDIES

The following briefly outlines the observed parameters of Kepler-444 and the analysis performed in B19.

2.1 Observations

The first asteroseismic study of Kepler-444 is that of Campante et al. (2015), who determined individual oscillation modes and parameters from the *Kepler* light curve. The large frequency separation was

determined to be $\Delta\nu = 179.64 \pm 0.76 \mu\text{Hz}$ and the frequency of maximum power to be $\nu_{\text{max}} = 4538 \pm 144 \mu\text{Hz}$. Additionally, they used spectroscopic measurements from the Keck I telescope and HIRES spectrograph (Vogt et al. 1994) to determine the effective temperature T_{eff} , surface gravity $\log g$, and elemental abundances. Using these in the stellar modelling, they determined the star to be an old star with sub-solar mass.

Mack et al. (2018) has since performed a spectroscopic study of the star using higher resolution spectra obtained with the Potsdam Echelle Polarimetric and Spectroscopic Instrument (PEPSI, Smitha & Solanki 2017). From this they determined the effective temperature $T_{\text{eff}} = 5172 \pm 75 \text{ K}$, the metallicity $[\text{Fe}/\text{H}] = -0.52 \pm 0.12 \text{ dex}$, and the alpha-enhancement $[\alpha/\text{Fe}] = 0.23$ which are all used in this paper.

The asteroseismic observations of Kepler-444 used in this work are those provided in Davies et al. (2016). These include the frequencies of the individual oscillation modes and a quality estimation of these. While all determined frequency modes are reported, the quality assurance check flagged the two modes $\nu(\ell = 2, n = 24, 25) = (4752.43 \mu\text{Hz}, 4932.4 \mu\text{Hz})$ to be more likely to be noise in the data than detected frequency modes (i.e. prior dominated). These are referred to as the flagged modes (FM) in the following analysis where their inclusion will be varied. While they are flagged due to the quality estimation, it is also important to notice that they form the two highest r_{02} frequency ratios, who are susceptible to shifts due to magnetic activity, as detailed by Thomas et al. (2021). They may therefore also be unreliable due to this effect, so varying their inclusion is also relevant due to this.

The frequencies are corrected for the Doppler shift arising from the line-of-sight velocity of the star V_r in accordance with Davies et al. (2014), who derived the correction to be a factor of $(1 + V_r/c)$ with c being the speed of light. The frequency ratios are calculated according to Eqs. (1) to (3) using 10 000 Monte Carlo realisations to determine their correlations (see section 4.1.3 of Aguirre Børsen-Koch et al. 2022; Verma et al. 2022).

With the recent data release from the Gaia mission (DR3, Gaia Collaboration et al. 2016, 2022), the line-of-sight velocity of Kepler-444 is measured to be $V_r = -120.784 \pm 0.255 \text{ km s}^{-1}$. This also provides high-accuracy measurements of the parallax $\varpi = 27.358 \pm 0.012 \text{ mas}$, the corresponding zero-point offset of $-20.468 \mu\text{as}$ (derived using the `gaiadr3-zeropoint` package, Lindgren et al. 2021), along with its coordinates. The observed magnitudes that will be used in conjunction with these are that of the Tycho-2 catalogue (Høg et al. 2000a,b), which provides the apparent magnitudes $B_T = 9.898 \pm 0.024$ and $V_T = 8.925 \pm 0.015$.

Across the previous asteroseismic studies of Kepler-444 (Campante et al. 2015; Silva Aguirre et al. 2015; Buldgen et al. 2019), they all determine fundamental stellar properties that agree within their uncertainties. It is determined that it has an age of $\sim 11 \pm 1 \text{ Gyr}$, has a mass of $\sim 0.748 \pm 0.044 M_{\odot}$ and a radius of $\sim 0.75 \pm 0.01 R_{\odot}$.

2.2 Forward modelling from B19

The modelling in B19 was performed in three steps (G. Buldgen, private communication). Firstly, they used the AIMS software (Rendle et al. 2019) to match the observations to a pre-calculated grid of models using a single set of input physics. Secondly, using the best-fit and neighbouring models from this, they used inversions of stellar structure to determine a precise measurement of the mean density of Kepler-444. Finally, with this constraint on the mean density together with the observed parameters described in the following paragraph, local minimisation was then performed with varying input physics,

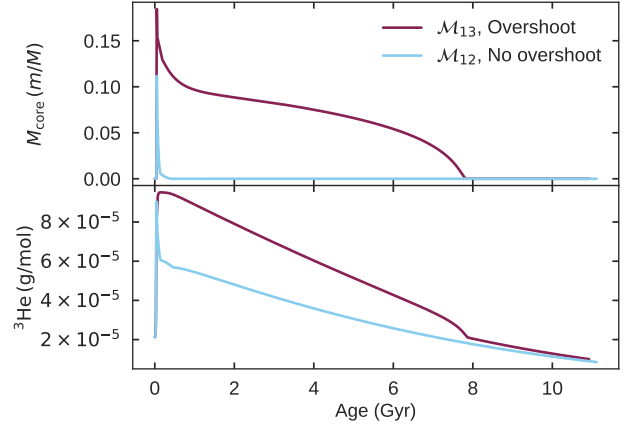


Figure 1. The evolution of \mathcal{M}_{12} (blue) and \mathcal{M}_{13} (red) in terms of the convective core size (top) and ^3He abundance (bottom). For \mathcal{M}_{13} the convective core is clearly quite extensive until 8 Gyr coinciding with its surplus of ^3He , while \mathcal{M}_{12} follows the predicted evolution with the helium content approximately equal to the equilibrium amount for the full evolution (Appendix A). Source: Reproduction of (Buldgen et al. 2019, fig. 7), data from G. Buldgen, private communication.

in order to obtain a better best fit model. The minimisation was executed using a Levenberg-Marquardt algorithm (Levenberg 1944; Jakeš 1988), while the models were computed on-the-fly using the Liège stellar evolution code (CLES, Scuflaire et al. 2008a) and the Liège stellar oscillation code (LOSC, Scuflaire et al. 2008b).

They determined the observed frequency ratios from the individual frequencies from Campante et al. (2015). While the same modes were available as those in Davies et al. (2016), quality estimations of the frequencies were not provided, and B19 did therefore not exclude the two flagged modes $\nu(\ell = 2, n = 24, 25)$. They performed minimisation of the χ^2 error function in regards to the r_{02} frequency ratios, $[\text{Fe}/\text{H}]$, T_{eff} , $\log g$, an estimated mean density $\rho = 2.495 \pm 0.050 \text{ g cm}^{-3}$, and a self-derived value of the photometric luminosity $L_{\text{phot}} = 0.40 \pm 0.04 L_{\odot}$ from a combination of Gaia DR2 and 2MASS observations. This was done across varying choices of input physics (equation of state, opacity tables, etc.) used for the models, which produced 13 different combinations of results (see tab. 1 of Buldgen et al. 2019). The determined parameters agreed within 1σ across all the combinations. However, of these 13 resulting models, the last two models, here referred to as \mathcal{M}_{12} and \mathcal{M}_{13} , are of interest in this work as they had the lowest overall χ^2 values. These models have been obtained from G. Buldgen (private communication) for the analysis and comparisons presented in this work. The determined properties of \mathcal{M}_{12} were a mass of $0.753 \pm 0.018 M_{\odot}$, an age of $11.13 \pm 0.57 \text{ Gyr}$, an initial hydrogen mass fraction $X_{\text{ini}} = 0.746$, and an initial metal mass fraction $Z_{\text{ini}} = 0.0076$. Similarly, the mass, age, X_{ini} and Z_{ini} for \mathcal{M}_{13} were determined to be $0.755 \pm 0.020 M_{\odot}$, $10.95 \pm 0.61 \text{ Gyr}$, 0.750 and 0.0069 respectively.

It was determined that \mathcal{M}_{13} had a lower χ^2 value than \mathcal{M}_{12} , and it is worth noting that this difference in χ^2 is mainly attributed to the comparison of the frequency ratios. The main difference in input physics between these models were that the treatment of convective overshoot was included in \mathcal{M}_{13} , while it was not included for \mathcal{M}_{12} . This resulted in the convective core mass fraction evolving quite differently for these two models as shown in Fig. 1. While they are both initially fully convective, \mathcal{M}_{13} has a substantial convective core that survives until $\sim 7.85 \text{ Gyr}$, while the convective core of \mathcal{M}_{12}

completely disappears after the first brief fully convective phase. This therefore appears to be an unconventional result as theory predicts that M_{12} would be the best model as sub-solar mass stars generally do not have convective cores during main-sequence evolution. As the result was based on the better fit of frequency ratios, and these are constructed to be sensitive to the interior structure of the star, it was therefore concluded that M_{13} provides the best prescription for the evolution of Kepler-444's convective core. It is this result which will be studied in this work.

The main difference between the stellar evolution code used in B19 and the code used in this work (see Section 3.1) lies in the mathematical prescription of convective overshoot. B19 used a step overshooting prescription that extends the boundary of the convective core as determined by the Schwarzschild criterion (Kippenhahn et al. 2012) by an amount depending on the local pressure scale height and a free (hyper)parameter α_{ov} (Scuflaire et al. 2008a, sec. 3.5). This extended region is thereby treated as a fully convective zone with instantaneous mixing. On the other hand, in this work we use exponential overshooting and treats mixing in all convective zones as diffusive (for a comprehensive comparison of the methods see Pedersen et al. (2018), section 2.1 and 2.2).

The presence of convective overshoot were shown by B19 to increase the abundance of ^3He compared to the equilibrium amount (see Appendix A), which were thus concluded to have caused an extended lifetime of the convective core. The correlation can clearly be seen in Fig. 1 (and Fig. A1) and is indeed the cause of the extended lifetime of the convective core in the models as was also shown in a previous study by Deheuvels et al. (2010). However, while the mixing was modelled using convective overshoot, it was not known whether this or alternative phenomena such as rotation was the true cause that produced the additional mixing. It is here worth noting that an extended convective-core lifetime in the models of B19 might also be partly induced from assuming instantaneous mixing of the convective zones. As mentioned in Zhang et al. (2022), this would require extreme convective velocities in the core, in order to fully mix before their nuclear consumption time.

3 GRID-BASED MODELLING

We use the so-called *grid-based* modelling approach. Here a grid of stellar models spanning the suitable parameter space is computed and the likelihood of the models are evaluated given a set of observations. Due to the unsolved degeneracies in the stellar models (for an overview, see Basu & Chaplin 2017), multiple configurations of stellar properties can yield high likelihoods when compared to the observed data. This grid-based method allows us to better get an overview of the different islands of probability or overall different solutions of sets of stellar properties that fit the observations. This method also allows for fitting different sets of observations without the cost of recomputing new models, which can be especially costly for the high-dimensional parameter space used in this work (see Section 3.2). An in-house code package¹ is used to construct these grids, which utilises the Sobol quasi-random, low-discrepancy sequences to uniformly populate the parameter space (Sobol & Levithan 1976; Sobol 1977; Antonov & Saleev 1980; Fox 1986; Bratley & Fox 1988; Joe & Kuo 2003).

The stellar evolution models are computed using GARSTEC (Weiss

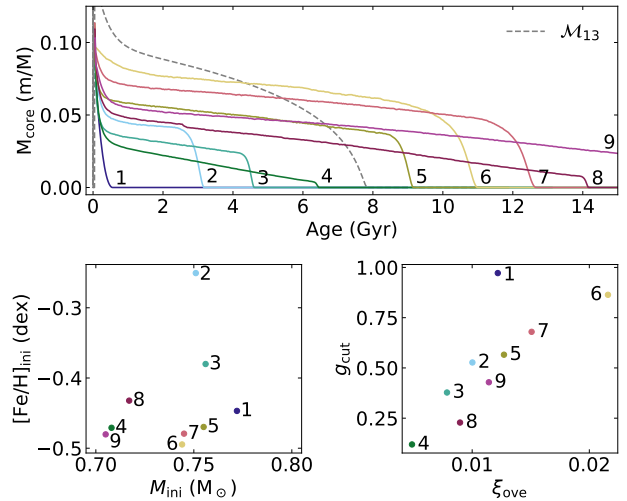


Figure 2. *Top:* Fractional mass of the convective cores as a function of age for stellar evolution tracks with varied combinations of overshooting efficiency f_{ove} and cut-off coefficients g_{cut} . The numbers label the tracks at the point their convective core disappears (τ_{core}) within the plotting range. *Bottom left:* Initial mass and metallicity of the tracks. *Bottom right:* Overshooting efficiency and cut-off coefficient of the tracks.

& Schlattl 2008). The code utilises a combination of the equation of state by the OPAL group (Rogers et al. 1996; Rogers & Nayfonov 2002), and the Mihalas-Hummer-Däppen equation of state (Daepfen et al. 1988; Hummer & Mihalas 1988; Mihalas et al. 1988, 1990). Atomic diffusion of elements are treated following the prescription by Thoul et al. (1994). For the opacity, the compilations used are the high temperature opacities from the OPAL group (Rogers & Iglesias 1992; Iglesias & Rogers 1996) and the low temperature opacities from Ferguson et al. (2005). The NACRE (Angulo et al. 1999) cross sections are used for the nuclear energy generation rate, except for the $^{14}\text{N}(p, \gamma)^{15}\text{O}$ and $^{12}\text{C}(\alpha, \gamma)^{16}\text{O}$ reactions that are instead from Formicola et al. (2004) and Hammer et al. (2005) respectively. The theoretical oscillation frequencies of the models are computed using the Aarhus adiabatic oscillation package (ADIPLS, Christensen-Dalsgaard 2008). For the computation of synthetic magnitudes the bolometric corrections of Hidalgo et al. (2018) are used in order to fit the parallax.

Due to Kepler-444 being α -enhanced, the element abundances have to be corrected accordingly. The stellar mixtures used are calculated based on the solar mixture from Asplund et al. (2009), by uniformly varying the relative abundance of the α -elements in steps of 0.1 dex in $[\alpha/\text{Fe}]$ (see Aguirre Børsen-Koch et al. 2022, section 3.2). The opacity tables are also updated taking the new abundances into account.

3.1 Convective overshooting and the geometric cut-off

As mentioned previously, several different implementations of convective overshooting exist. The implementation used in this work is the default option in the stellar evolution code GARSTEC. It treats overshooting as a diffusive process with the diffusion constant D at a distance z outside the convective zone being

$$D(z) = D_0 \exp\left(-\frac{2z}{f_{ove}\bar{H}_P}\right), \quad (5)$$

¹ Planned for eventual public release accompanying the BASTA-code: <https://github.com/BASTAcode>

where \tilde{H}_P is the so-called modified pressure scale height (see below), D_0 is the diffusive constant taken just inside the convective zone, and f_{ove} is the convective overshoot efficiency parameter, which is a dimensionless, free parameter of the model.

The pressure scale height H_P is locally modified to adjust the convective overshoot in correspondence with the size of the convective zone. It is scaled by the so-called geometric factor G , which is defined as

$$G = \left(\frac{R_{\text{cz}} f_{\text{ove}}}{g_{\text{cut}} H_P} \right)^2, \quad (6)$$

where R_{cz} is the radial thickness of the convective zone, and g_{cut} is the dimensionless cut-off coefficient. By default in `GARSTEC`, the cut-off coefficient is set to produce the expected behaviour for the evolution of convective core in the Sun, which initialises it to $g_{\text{cut}} = 2$, but will here be treated as a free parameter in order to artificially induce longer convective-core lifetimes. To only reduce the amount of overshoot and not amplify it, \tilde{H}_P is determined as

$$\tilde{H}_P = \begin{cases} H_P & \text{if } G \geq 1 \\ GH_P & \text{if } G < 1 \end{cases}. \quad (7)$$

For low-mass stars and $g_{\text{cut}} = 2$ this results in the expected behaviour where no convective core is present after the first ~ 200 Myr of evolution. On the other hand, lower values can result in convective overshoot to not be limited ($G \geq 1$), and thus allows for the core to be fed additional ${}^3\text{He}$. This increases energy production and thus extends the lifetime of the convective core (see Appendix A). It will however still contract, but at a slower pace.

When the core has contracted to the point where $G < 1$, the extent of the convective overshoot will be reduced following Eqs. (5) and (7). Due to this, the amount of material the core is fed will also reduce, in turn causing further contraction of the convective core, and a reduction of the extent of the convective overshoot. This is therefore a self-reinforcing effect, which means that when the geometric cut-off is triggered, it will cause an exponential decrease in convective core size.

Fig. 2 demonstrates how the convective core evolution depends on f_{ove} and g_{cut} . Their evolution is summarised in terms of the convective-core lifetime τ_{core} , defined as the age where the convective core mass fraction first decreases below 10^{-4} . Should the track end before this point, the core lifetime is estimated from a linear extrapolation to the last 50 models in the track, up to a maximum of 20 Gyr. The correlations between f_{ove} and g_{cut} in Fig. 2 (bottom right panel), in relation to the convective core, can be described as follows:

- The center of the plot shows models with a birth early convective core that disappears before its current age, and is thus the region where core evolution can be similar to that of \mathcal{M}_{13} ,
- low values of f_{ove} never produce convective cores of any significant size,
- large values of f_{ove} but high values of g_{cut} produce a significant convective core that disappears rapidly (< 1 Gyr),
- large values of f_{ove} but low values of g_{cut} produce a significant convective core that does not disappear before the current stellar age.

While the whole parameter space shown in Fig. 2 (bottom right panel) is sampled in the final grid, the tracks shown in the figure were selected to show a step-variation of τ_{core} , and it is therefore a biased selection. With enough variations of these hyper parameters, it should be possible to infer whether or not Kepler-444 has had a convective core during its lifetime.

Table 1. Varied parameters of the grid with 3000 tracks. The sampling is demonstrated in Appendix C.

Variable	Minimum	Maximum
M (M_{\odot})	0.70	0.80
$[\text{Fe}/\text{H}]_{\text{ini}}$	-0.55	-0.25
Y_{ini}	0.24	0.27
$[\alpha/\text{Fe}]$	0.2	0.3 ^(a)
α_{MLT}	1.60	2.00
f_{ove}	0.00	0.03
g_{cut}	0.1	1.0

^(a) Opacity tables have only been computed in steps of 0.1, so only the two values are available in the grid.

3.2 Free parameters

In this work, we use 7 free (initial) parameters for constructing the grid of models. They consist of the stellar mass, the parameters describing the composition of the star, and the (hyper) parameters of the hydrodynamics.

The composition of stars are determined from the initial metallicity $[\text{Fe}/\text{H}]_{\text{ini}}$, the enhancement of alpha element abundance $[\alpha/\text{Fe}]$, and the initial helium mass fraction Y_{ini} . The initial hydrogen abundance X_{ini} and metal abundance Z_{ini} is derived from these and the solar metal to hydrogen mass fraction $(Z/X)_{\odot}$ of the given abundance table.

In one-dimensional models, the treatment of hydrodynamics is prescribed through the approximate mixing-length theory (MLT, [Böhm-Vitense 1958](#)). It depends on the mixing-length parameter α_{MLT} , which describes the length ℓ over which a convective element inside the Schwarzschild border moves,

$$\ell = \alpha_{\text{MLT}} H_P. \quad (8)$$

As it is not possible to derive the value of this parameter from first principles, it can either be calibrated to the solar value and assumed to be constant for all stars, or be allowed to vary as a free parameter. In this work, the latter approach is chosen. Additionally, the hyperparameters prescribing the convective overshoot, the already mentioned overshooting efficiency f_{ove} and the cut-off coefficient g_{cut} , are also varied.

In total, these 7 free parameters will be varied when constructing the grid (as seen in Table 1 and the following subsection). The number of free parameters is considered when deciding upon the number of tracks in the grid in order to ensure a well distributed sampling along each dimension.

3.3 The grid of stellar models

The grid of stellar models used to infer stellar properties of Kepler-444 consists of 3000 stellar evolution tracks. The intervals of the parameters describing the tracks are given in Table 1, and their variation is determined as described in the beginning of this section. Due to the multidimensional quasi-random designation of parameters, the best way to evaluate the occupancy of the parameter space is to determine the volume w each point occupies in this space, which is then used to compute the Bayesian posterior (see Section 3.4). The occupancy is also shown in Appendix C.

The range of models in a given track is limited between the zero-age main-sequence and when the model reaches a large frequency separation of $\Delta\nu = 170 \mu\text{Hz}$. Here, the zero-age main-sequence is determined as where the ratio between the hydrogen burning lumi-

nosity and the total luminosity reaches 1. The maximum time step is between 20 and 40 Myr, depending on initial mass. Synthetic magnitudes are computed for the Tycho-2 photometric system and used for fitting the parallax, ϖ (for more details, see section 4.2.2 in Aguirre Børsen-Koch et al. 2022). The grid has been computed with atomic diffusion enabled.

Across the subset of parameter space spanned by f_{ove} and g_{cut} , the size of the convective core can have varied initial sizes and evolve in a lot of different ways as demonstrated in Fig. 2. Thus the grid has models available for all possible sizes and lifetimes of the early convective core, with a minimum $\min(\tau_{\text{core}}) = 0.139$ Gyr and a maximum, as described in Section 3.1, of $\max(\tau_{\text{core}}) = 20$ Gyr. The grid contains 400 tracks with a convective-core lifetime $\tau_{\text{core}} = [1, 9]$ Gyr.

3.4 Fitting algorithm

To match the observations to the models, we use the BAYesian STellar Algorithm (BASTA, Silva Aguirre et al. 2015; Aguirre Børsen-Koch et al. 2022, ²). It uses Bayes' theorem to combine prior knowledge about the stellar parameters Θ with the data D to give the likelihood $P(D|\Theta)$ of observing the data given the model parameters. The total likelihood is the product of the likelihood of individual groups of observables, D_i , determined as

$$P(D_i|\Theta) = \frac{1}{\sqrt{2\pi}|\mathbf{C}_i|} \exp\left(-\chi_i^2/2\right), \quad (9)$$

where $|\mathbf{C}_i|$ is the determinant of the covariance matrix, and

$$\chi_i^2 = \frac{1}{N_i} (\mathbf{O}_{i,\text{obs}} - \mathbf{O}_{i,\text{mod}})^T \mathbf{C}_i^{-1} (\mathbf{O}_{i,\text{obs}} - \mathbf{O}_{i,\text{mod}}), \quad (10)$$

is the chosen error function, where N_i is the number of observables in the group, $\mathbf{O}_{i,\text{obs}}$ is the observed values of parameters in the group, and $\mathbf{O}_{i,\text{mod}}$ likewise for the model. Also included in the posterior is the prior information, here only the initial mass function (Salpeter 1955). To marginalise the posterior probability, the weight of the model is taken into account. This weight is the product of the volume w it occupies in the parameter space used to construct the grid (see Section 3.3), and a measure of how much volume a model occupies along a track. The latter is determined from the difference in ages of the tracks, and therefore represents a measure of evolutionary speed (Jørgensen & Lindegren 2005) (for a more detailed description of these calculations, see Aguirre Børsen-Koch et al. (2022), section 2).

The resulting marginalised posterior has no predetermined form, but instead accurately depicts the probability distribution for each parameter. This also means that more than one solution can appear, and one therefore needs to look at the posterior distributions to get a complete picture of the solution. To represent the distribution, the inferred parameters are traditionally reported in terms of the median value, and the 16 and 84 percentiles of the distribution, which is known as the 68% Bayesian credible interval.

One can also look at the best-fit model to evaluate properties such as the fit to the observed ratios. Here it is necessary to make the distinction between the two ways we define the best-fit model. Based on the computation of likelihood as just described, the *highest-likelihood model* (HLM) can be extracted as the best-fit model. The second is the *lowest- χ^2 model* (LCM) as determined by the error function Eq. (10), which is independent of the grid. The LCM definition of the best-fit model were also used in B19 and will be used for comparison between these works (see Section 5).

² Available at: <https://github.com/BASTAcode/BASTA>

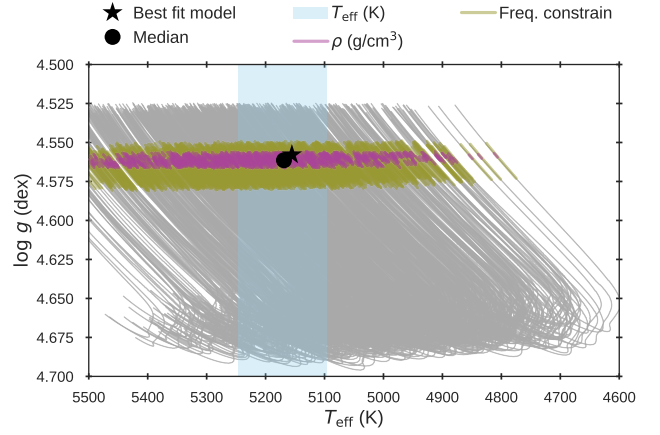


Figure 3. Kiel diagram of the fitted parameters across the evolutionary tracks in the grid. It shows the observational constraints of the fitted parameters within each track, as well as the median and best-fit model of the fit. The frequency constraint is described in the text, while the constraint from the observed metallicity is not shown as it barely changes along the track, but only tracks with models with a metallicity within the determined Bayesian credible interval is shown.

A prominent advantage of using BASTA is its versatility. It can handle the multitude of different observables needed in this study, which allows for testing of each observation's impact on the convective-core lifetime, which we will do in the following.

4 RESULTS

Here our independent study of Kepler-444 is presented, both in terms of the overall determination of the properties of the star, and a deeper dive into the convective-core lifetime. Throughout this section, the HLM definition of the best-fitting model is used.

4.1 General fit

Here, we present the results of fitting the set of observables ($[\text{Fe}/\text{H}], T_{\text{eff}}, r_{012}, \rho$). The usual chosen set of observables in BASTA does not include ρ , as it is not readily observable, but is included here as an additional constraint on the interior structure derived from the individual frequencies. For testing and comparison, the full set as used in B19 as well as different sets of observables and definitions of the frequency ratio fit have been explored. These are presented in Section 5.

As described in Section 2.1, the two frequency modes $\nu(\ell = 2, n = 24, 25)$ have been flagged as unreliable. They have therefore been omitted in the following, whereby the two frequency ratios $r_{02}(\nu = 4752.43 \mu\text{Hz}, 4932.4 \mu\text{Hz})$ are not included in the fit. These are referred to as the flagged modes (FM) in the following sections. The implications of this is explored further in Section 5, as that were not the case for B19.

The results are presented in Figs. 3 and 4. Fig. 3 shows how the observed parameters overlap with the models in the grid by colouring the models with parameters within the observed limits. The frequency constraint in the figure is determined from matching the lowest $\nu(\ell = 0)$ mode in the observations to the models in the grid. Only models having a frequency difference of this mode within $\pm 0.5\Delta\nu$ are considered when calculating the likelihood, and it is this

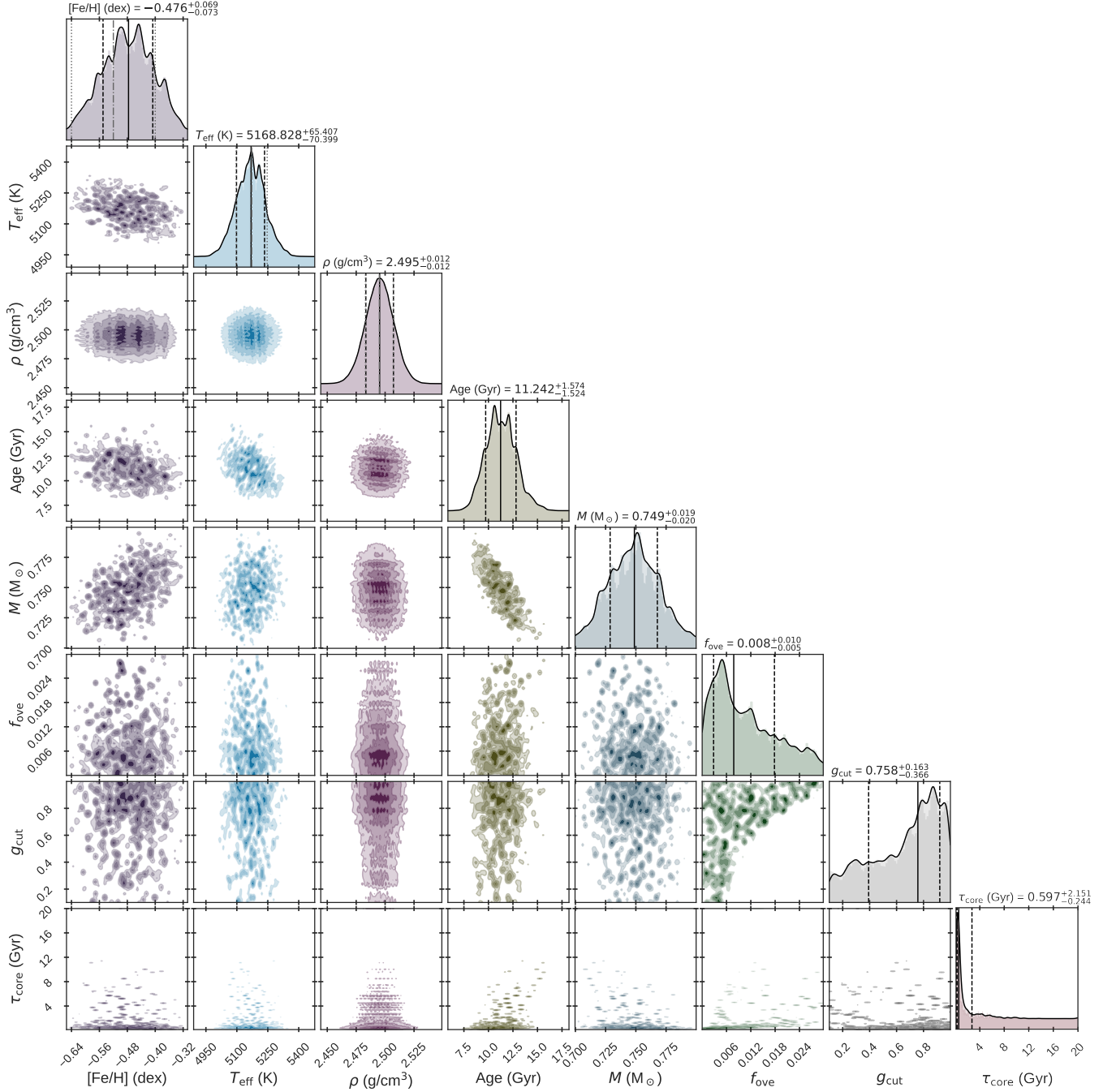


Figure 4. Corner diagram of the fitted and inferred parameters. The values are given (and shown in the diagonal panels) as the median (solid black line) and the 16th and 84th percentiles (dashed black lines) of the posteriors. On the diagonal, the grey lines give the observed value (dash-dotted) with their uncertainties (dotted) for the fitted observables.

selection that is highlighted in Fig. 3. Also shown is the median of the marginalised posterior shown in Fig. 4, and the best-fit model (here the HLM). Figure 3 shows that the observational constraints converge at a broad selection of models. While the constraints from the observed parameters are quite broad, compared to the resolution of the grid, the deviation of the best fit model from the median arises from the fit of ratios.

The marginalised posterior distributions of the fitted and inferred stellar properties are shown in the diagonal panels of Fig. 4, while

2-dimensional (2D) histograms of the likelihood between the parameters are shown in the remaining panels. The solution is in agreement with the previous studies of Kepler-444 as presented in Section 2.1 and the fitted non-frequency parameters match well within their observed uncertainties. The posterior distributions mostly show unimodal distributions, so the properties are well constrained. It determines τ_{core} to be $0.597^{+2.151}_{-0.244}$ Gyr, with the 14th percentile being twice the minimum available τ_{core} of 0.139 Gyr.

The 2D-histogram between f_{ove} and g_{cut} , (green histogram on

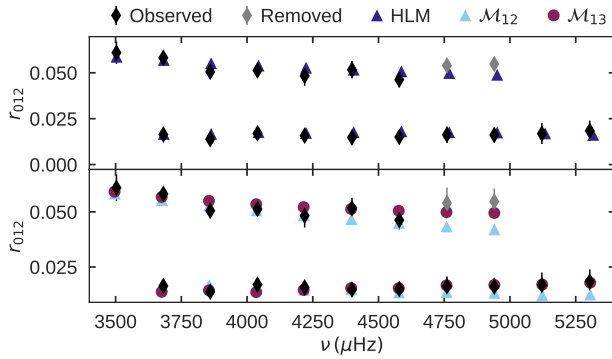


Figure 5. The r_{012} frequency ratio sequence of the observed frequencies compared to the best-fit model using BASTA (*top*), and the M_{12} and M_{13} models from B19 (*bottom*). The lower sequence in both panels is the r_{01} ratios, while the upper sequence is the r_{02} ratios, where the flagged modes r_{02} ($n = 25, n = 26$) are shown in grey.

the second-to-last row, sixth column) from the bottom left in Fig. 4, clearly shows no islands of probability in the lower-right region. Comparing this with the interpretation presented in Section 3.1, it clearly shows close-to-zero likelihood for any model that has a large convective core surviving until its current age. Meanwhile, the correlation does not directly describe the lifetime of a convective core that has disappeared before the current age. However, as can be seen from the τ_{core} histogram in Fig. 4 (bottom right panel), the fit does infer a short-lived convective core.

4.2 Best-fit models

Shown in Fig. 5 is the ratios of the HLM compared to the observed ratios alongside the ratios of M_{12} and M_{13} . It can be seen that the flagged modes show a clear deviation from the r_{02} sequence, being greater than the extrapolation of the sequence would predict. We here emphasise that the offset between the modes on the x-axis in the top panel is caused by only fitting the ratios and not the individual frequencies. The échelle diagrams of the HLM are shown in Appendix B.

In order to get a better understanding of the inferred τ_{core} , we look into the convective core evolution of the best 5 tracks, defined by comparing the HLM within each track and here simply numbered using # with #1 being the best track using this metric. The convective core evolution of these 5 best tracks compared to M_{13} is shown in Fig. 6. It shows that it is not dominated by the expected interpretation of $\tau_{\text{core}} < 1$ Gyr, but rather shows a spread around the upper limit. This indicates that the ratios do not provide a large enough constraint on the early convective core to differentiate between these values of τ_{core} . This might be due to how the prolonged τ_{core} is modelled or the precision of the observed modes, but it is more likely that τ_{core} is a parameter not generally well-constrained by the ratios, which is discussed further in Section 5.2.

To explore this spread in τ_{core} of the HLM's, the tracks with the largest difference in τ_{core} among these 5 best-fitting tracks in Fig. 6, track #2 with the lowest τ_{core} and track #4 with the highest, are explored in more detail. As the modelled ratios are effectively a function of the sound speed c_s in the stellar interior and thereby the profile in chemical composition of the model (Aerts et al. 2010), looking at these profiles should give some understanding of the issue

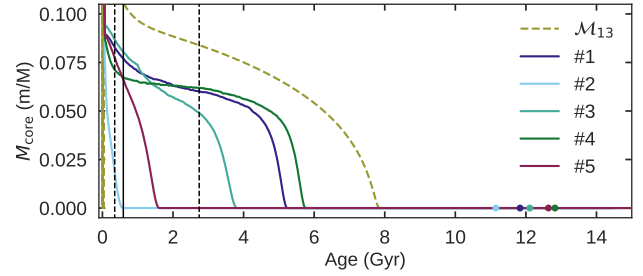


Figure 6. Convective core mass fraction as a function of age for the 5 best-fitting tracks determined from comparing the HLM within each track. The dots indicate the HLM within each track, while the black vertical lines show the inferred median (solid) and 16th and 84th percentile (dashed) τ_{core} from the posterior (bottom right panel of Fig. 4).

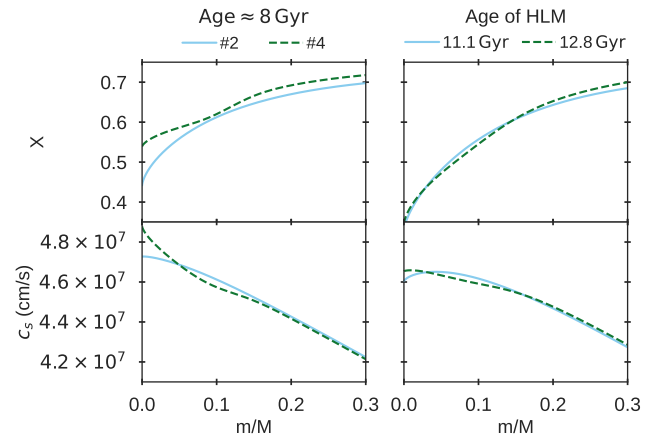


Figure 7. The local hydrogen mass fraction (*top*) and sound speed (*bottom*) profiles as a function of mass of the two tracks with the greatest difference in core lifetime from Fig. 6. *Left*: The profiles of models within the track at ≈ 8 Gyr. *Right*: The models within the track with the highest likelihood (HLM, highest likelihood model), at the age given in the legend.

in constraining τ_{core} . The difference between the local hydrogen mass fraction X and sound speed profile of the two tracks are shown in Fig. 7 at an age of 8 Gyr and at the age of their respective highest likelihood model. While it is apparent at 8 Gyr that track #4 still carries a signature of a convective core in both profiles, it is no longer apparent at the HLM, where it is similar to the short τ_{core} track.

The highest likelihood model of track #4 is however much older than that of #2. This indicates that a reason why large τ_{core} models in the fit have an adequately high likelihood is that they have evolved for longer until the traces of the convective core has essentially disappeared from their interior structure. As the frequency ratios are the best parameter for constraining the age within the available observations, this allows for the inference of older models, compared to low τ_{core} models, which obtain a profile without traces of a convective core much earlier. It is also apparent in Fig. 6, as the age of the HLM somewhat scales with τ_{core} . This is also vaguely apparent in the 2D histogram between age and τ_{core} in Fig. 4 (bottom row, column 3), as a linear upwards trend, but is smeared out due to the degeneracy of the age with variation of the other parameters in the grid.

4.3 Additional models

The presented analysis has also been repeated using other models of varied input. The general results are here briefly summarised.

An equally extensive grid of models as presented in Section 3.3 without the inclusion of atomic diffusion, and an appropriately adjusted initial metallicity, has been tested. These models do however not reliably match the observations, as is expected, as it is generally accepted that diffusion is needed to produce realistic models of sub-solar mass stars (e.g. Christensen-Dalsgaard et al. 1993; Silva Aguirre et al. 2017; Sahlholdt et al. 2018).

To verify the approach of varying the geometric cut-off, as described in Section 3.1, two additional cases have been studied. The first case completely removes the geometric cut-off, which however allowed for convective cores to fluctuate in and out of existence throughout the whole evolution due to numerical effects. These were therefore not used for the analysis.

Additionally, while the default value of g_{cut} in the GARSTEC code is 2, the grid used in this analysis were chosen to have a maximum value of 1. This was selected based on initial tests with varying g_{cut} between 1 and 2 (along with a varying of f_{ove}), which were determined to only produce models with $\tau_{\text{core}} < 1$ Gyr. This interval would therefore be redundant to sample in the grid, and was therefore left out.

5 DISCUSSION

As the lifetime of the convective core we determined in Section 4 is different compared to that of B19, it is of interest to determine what leads to this difference. Here we vary the choice of observables to use in the fitting set and the choices related to fitting the frequency ratios and compare for both the method presented in this work and for \mathcal{M}_{12} and \mathcal{M}_{13} from B19 to determine their influence on τ_{core} .

The comparisons are based on comparing χ^2 values. As described in Section 3.4, these are also determined for each model in this work in accordance with Eq. (10), which can therefore be used to compare to the results of B19. For consistency, the model values and frequencies of \mathcal{M}_{12} and \mathcal{M}_{13} are here used to re-compute χ^2 values within the same framework. The mean density was, however, not available in the models, and have instead been estimated to be $\rho_{\mathcal{M}_{12}} = 2.4925 \text{ g cm}^{-3}$ and $\rho_{\mathcal{M}_{13}} = 2.4933 \text{ g cm}^{-3}$ from fig. 3 in B19.

The χ^2 determined from Eq. (10) is only for a given set of observables, where the correlations are known. For this study, this only includes the ratios as the correlations of the other observables are not known. Therefore, for transparency, the total χ^2 of a model is determined from the ratio contribution χ_r^2 calculated from Eq. (10) along with the remaining observables i as

$$\chi^2 = \chi_r^2 + \sum_i \left(\frac{O_{i,\text{obs}} - O_{i,\text{mod}}}{\sigma_i} \right)^2, \quad (11)$$

where σ_i is their observational uncertainty. Note that this implies that the contribution to the total value from the ratios are divided by the number of ratios (N_i in Eq. (10)), and are thus weighted equally with a single classical global parameter as is default in BASTA. It is possible to weigh each ratio as an individual measurement (Cunha et al. 2021; Verma et al. 2022), and the effect of this is detailed at the end of Section 5.2.

Finally, it is important to note here that B19 used the frequencies from Campante et al. (2015) to determine the frequency ratios, while we here only use the frequencies from Davies et al. (2016). The χ^2

values will therefore be close to, but not exactly the same values as in B19.

In the following, the variation of χ_r^2 will be discussed separately from the variation of the total χ^2 , which is discussed thereafter.

5.1 Impact of ratio fitting

The better χ^2 of the fit to the model with a convective core \mathcal{M}_{13} in B19 is attributed to the ratios. There are however several choices behind how the frequency ratios are fitted. Here, we explore these to determine how they affect the difference in χ_r^2 between the models.

While the r_{01} ratios in this work so far uses the five-point small frequency separations (Eq. (2)), one can also use the less correlated but also less smooth three-point small frequency separations (Eq. (4)). Both have been implemented and will be compared, referred to as the $5p$ and $3p$ cases respectively. Secondly, it is varied whether the two uncertain ratio modes r_{02} ($n = 25, 26$) flagged by Davies et al. (2016) are included. It is apparent from Fig. 5 that these modes match \mathcal{M}_{13} better than \mathcal{M}_{12} , so their inclusion is varied in order to compare the influence on the fit. Lastly, it is varied whether the covariance \mathbf{C}_r of the determined ratios has been taken into account or not. Frequency ratios are by design correlated as they are computed from the same set of mode frequencies so this can have a large impact.

Our calculated χ_r^2 values of \mathcal{M}_{12} and \mathcal{M}_{13} for all the combinations of the above mentioned choices are compared in Table 2, where case 5 corresponds to the choices made in B19. As shown, the conclusion that the ratios favour \mathcal{M}_{13} over \mathcal{M}_{12} is only recovered for cases 5, 7, and 10, and can be attributed to two effects. Firstly, it is only recovered when the two flagged frequency modes are included in the set of frequencies, demonstrating the importance of well-determined mode frequencies, outside of their reported uncertainties. The other effect is the inclusion of covariance in the computation as it generally increases the χ^2 value due to the ratios being highly correlated by construction, comparing e.g. case 9 to 13, and 11 to 15. The increase in χ^2 value is also larger for \mathcal{M}_{13} than \mathcal{M}_{12} .

However, when looking at the r_{01} sequence exclusively, it becomes obvious that the χ^2 contribution of the mode r_{01} ($n = 21$) dominates the χ_r^2 for \mathcal{M}_{13} , due to its small observational uncertainty, while the corresponding mode of \mathcal{M}_{12} also deviates relatively much. Here we explore how the results are affected by this mode. The fitting case $\mathcal{M}_{13}^{\#21}$ is introduced where this mode is excluded from the χ_r^2 computation. The last two columns in Table 2 shows the comparison between the χ_r^2 of \mathcal{M}_{12} and \mathcal{M}_{13} for this case, for all of the combinations of fitting ratios described before. It shows that the r_{01} sequence fits \mathcal{M}_{13} much better when excluding this mode, which is also reflected in some cases of fitting the full r_{012} sequence. However, the conclusion for our preferred fitting case (case 16) remains unchanged, although the difference in χ^2 between the models is significantly lower.

Therefore, the combined choices of inclusion of the flagged modes and not fitting the covariance in the ratio fitting appear to cause the preference of \mathcal{M}_{13} over \mathcal{M}_{12} . In our preferred choice of the ratio fitting framework, case 16, we therefore find \mathcal{M}_{12} to be a better fit to the observations than \mathcal{M}_{13} based on the frequency ratios alone.

5.2 Choice of fitting parameters

To make a realistic comparison to the work of B19, and determine the influence on the inferred τ_{core} , we repeat the fit presented in Section 4 using different combinations of fitting sets and ratio fitting choices.

First of all, to test whether a sufficient density of the grid has been reached, the fit from Section 4 has been repeated using only

Table 2. Our calculated χ_r^2 values of \mathcal{M}_{12} and \mathcal{M}_{13} for the 16 different cases of fitting the ratios, where the lowest value is highlighted in bold font. The “Seq.” column denotes the frequency ratio sequence fitted. The $3p/5p$ column denotes whether the three- or five-point definitions of the small frequency separations (Eqs. (2) and (4) respectively) have been used, and it is left blank when fitting the r_{02} sequence as it does not change depending on this definition. The FM (Flagged Modes) column denotes when the two ratios r_{012} ($n = 25, 26$) have been excluded, while crossed out when they are included and left blank for the r_{01} sequence as they are not used for this sequence. The “Cov.” column denotes when the covariance of the frequency ratios has been taken into account in the χ_r^2 calculation and crossed out when the correlations are not taken into account. The last two columns lists the χ_r^2 for the \mathcal{M}_{01}^{21} case, see text for details.

Case	$\chi_r^2(\mathcal{M}_{12})$	$\chi_r^2(\mathcal{M}_{13})$	Seq.	$3p/5p$	FM	Cov.	$\chi_r^2(\mathcal{M}_{12}, \mathcal{M}_{01}^{21})$	$\chi_r^2(\mathcal{M}_{13}, \mathcal{M}_{01}^{21})$
1	1.111	1.518	r_{01}	$3p$		x	0.721	0.484
2	1.070	1.284	r_{01}	$5p$		x	0.743	0.170
3	1.083	1.426	r_{01}	$3p$		✓	0.666	0.364
4	1.446	1.908	r_{01}	$5p$		✓	0.686	0.219
5	1.215	0.942	r_{02}		x	x	1.225	0.926
6	0.403	0.942	r_{02}		✓	x	0.411	0.967
7	1.234	0.922	r_{02}		x	✓	1.198	0.907
8	0.404	0.959	r_{02}		✓	✓	0.412	0.965
9	1.161	1.284	r_{012}	$3p$	x	x	0.940	0.670
10	1.141	1.110	r_{012}	$5p$	x	x	0.965	0.529
11	0.843	1.323	r_{012}	$3p$	✓	x	0.606	0.654
12	0.801	1.136	r_{012}	$5p$	✓	x	0.607	0.497
13	1.211	1.991	r_{012}	$3p$	x	✓	0.902	0.665
14	1.477	2.386	r_{012}	$5p$	x	✓	0.921	0.721
15	0.950	2.068	r_{012}	$3p$	✓	✓	0.578	0.630
16	1.168	2.515	r_{012}	$5p$	✓	✓	0.579	0.661

the first half (1500 tracks) of the grid. This fit did not determine a result noticeably different from what was obtained using the whole grid. We can therefore conclude that the grid has reached a sufficient density for convergence of the results.

For the tests using varied fitting sets, the results are summarised in Table 3, where the χ^2 values calculated for the HLM and LCM obtained with BASTA are compared to the corresponding χ^2 value for \mathcal{M}_{12} and \mathcal{M}_{13} . The determined τ_{core} from BASTA is reported alongside the χ^2 values, for comparison with the τ_{core} obtained in Section 4.

For fitting of non-asteroseismic parameters the determined values listed in Section 2.1 are used. The results in Section 4 were obtained by fitting the set ($[\text{Fe}/\text{H}], T_{\text{eff}}, \rho$), while the forward modelling approach of B19 did minimisation in regards to the set ($[\text{Fe}/\text{H}], T_{\text{eff}}, L_{\text{phot}}, \log g, \rho$). We explore the implications of using partly and fully the same set as B19 to determine their influence on the inferred τ_{core} , using the standard BASTA fitting set ($[\text{Fe}/\text{H}], T_{\text{eff}}$) as a baseline. Additionally, it is tested how adding a fit of the distance through the parallax and apparent magnitudes affects the result. As \mathcal{M}_{12} and \mathcal{M}_{13} does not include synthetic magnitudes, the distance have not been fitted to these models and their χ^2 values are thus not reported for this case.

The full set of possible ratio fitting choices as described in Section 5.1 has been repeated for the standard ($[\text{Fe}/\text{H}], T_{\text{eff}}$) fitting set, cases 1-16 in Table 3. For the remaining fitting sets, the recommended ratio fitting case as used in Section 4 (case 16 in Table 2) and the ratio fitting case with r_{012} but opposite choices of the remaining ratio fitting variations (case 9 in Table 2) are used throughout cases 17-30, 33 and 34 in Table 3. Case 31 fits the r_{02} sequence as was done in B19 along with their chosen classical parameters, while case 32 does the same, but with our recommendation of removing the flagged modes and including the covariance.

Overall, the LCM has the lowest χ^2 across all cases. This is primarily caused by the contribution from T_{eff} being higher for \mathcal{M}_{12} and \mathcal{M}_{13} . Comparing the χ^2 of these two models, only case 31 leads to \mathcal{M}_{13} having a lower χ^2 than \mathcal{M}_{12} . One would expect this to also be the case for fitting case 5 and 7, as the ratios for these cases were

determined to favour \mathcal{M}_{13} in Section 5.1. However, due to the normalisation of χ_r^2 , the total χ^2 is dominated by the contribution from T_{eff} , which deviates more for \mathcal{M}_{13} . The case of not normalising the ratios is discussed at the end of this section.

As can be seen across all fitting cases in Table 3, the inferred median τ_{core} is stable at ~ 0.6 Gyr for fits using the r_{01} ratios. The r_{02} ratios alone shows to have a poor inference power on this parameter, as expected since it has been shown to carry little information on the location of the convective zones (Roxburgh 2009). The upper bound (84th quantile of the posterior) vary more across fitting sets, but generally places an upper limit at ~ 3.5 Gyr. As was mentioned in Section 4.2 this large span in inferred values imply that the ratios most likely do not provide a direct constraint on τ_{core} . They however provide the best constraint on internal structure, and is thus the best available parameter to attempt to constrain τ_{core} .

Case 31 shows a preference of \mathcal{M}_{13} over \mathcal{M}_{12} when fitting as was done in B19, recovering their solution. Case 32 shows that by removing the flagged modes and taking covariances into account, the opposite preference of models are obtained. The determined 84th percentile on τ_{core} for both cases are twice as large as the cases fitting r_{012} , showing that this choice of fitting parameters provide a poor constraint on τ_{core} .

To verify the results using different photometric observations than those used in B19, the standard fitting case was repeated including the fitting of distance/parallax in cases 33 and 34 (method described in section 4.2.2 of Aguirre Børsen-Koch et al. 2022). It uses the Tycho-2 magnitudes, as mentioned in Section 2.1, as the Gaia-magnitudes were found not to converge at a solution within the grid. The results from these cases are consistent with the other cases, and thus the determined τ_{core} seems independent on the choice of photometric observables.

It is worth noting that the HLM and LCM models from the BASTA fits often have $\tau_{\text{core}} = 2 - 5$ Gyr. As described in Section 4 and Fig. 7, these are found to be older models where the signature of the convective core has almost disappeared from the profiles of the internal structure. While not immediately apparent in the determined ages (e.g. as given in Fig. 4), this could lead to a systematic increase in

Table 3. Comparison of χ^2 values between the fits using BASTA and the \mathcal{M}_{12} and \mathcal{M}_{13} models. HLM refers to the highest likelihood model in the BASTA fit and LCM refers to the lowest χ^2 model in the BASTA fit as introduced in Section 3.4. τ_{core} is the determined core lifetime from the fit. Fitting set describes the non-seismic fitted parameters, apart from [Fe/H] and T_{eff} which are always included in the fit. Their values and uncertainties are detailed in Section 2.1. The last four columns follow the same definitions as in Table 2.

Case	χ^2 (HLM)	χ^2 (LCM)	χ^2 (\mathcal{M}_{12})	χ^2 (\mathcal{M}_{13})	τ_{core} [Gyr]	Fitting set	Seq.	3p/5p	FM	Cov.
1	0.899	0.535	1.338	2.415	$0.631^{+2.700}_{-0.261}$		r_{01}	3p		x
2	0.772	0.485	1.297	2.180	$0.641^{+2.773}_{-0.264}$		r_{01}	5p		x
3	0.610	0.526	1.310	2.322	$0.631^{+2.778}_{-0.262}$		r_{01}	3p		✓
4	1.014	0.614	1.672	2.804	$0.631^{+2.706}_{-0.263}$		r_{01}	5p		✓
5	1.037	0.684	1.441	1.838	$0.767^{+6.366}_{-0.368}$		r_{02}		x	x
6	0.963	0.433	0.629	1.838	$0.713^{+5.307}_{-0.313}$		r_{02}		✓	x
7	1.029	0.681	1.461	1.819	$0.767^{+6.366}_{-0.368}$		r_{02}		x	✓
8	0.981	0.446	0.631	1.856	$0.713^{+5.307}_{-0.313}$		r_{02}		✓	✓
9	1.025	0.687	1.388	2.180	$0.634^{+2.779}_{-0.257}$		r_{012}	3p	x	x
10	0.980	0.677	1.367	2.006	$0.636^{+2.777}_{-0.256}$		r_{012}	5p	x	x
11	0.850	0.515	1.069	2.219	$0.635^{+2.465}_{-0.256}$		r_{012}	3p	✓	x
12	0.809	0.477	1.028	2.033	$0.634^{+2.466}_{-0.254}$		r_{012}	5p	✓	x
13	1.022	0.642	1.438	2.887	$0.624^{+2.438}_{-0.253}$		r_{012}	3p	x	✓
14	1.139	0.734	1.703	3.283	$0.613^{+2.329}_{-0.243}$		r_{012}	5p	x	✓
15	0.809	0.466	1.177	2.965	$0.622^{+2.195}_{-0.245}$		r_{012}	3p	✓	✓
16	0.894	0.527	1.395	3.412	$0.625^{+2.123}_{-0.248}$		r_{012}	5p	✓	✓
17	2.003	1.489	1.846	2.288	$0.631^{+2.548}_{-0.260}$	L_{Phot}	r_{012}	3p	x	x
18	1.938	1.500	1.853	3.519	$0.609^{+2.074}_{-0.239}$	L_{Phot}	r_{012}	5p	✓	✓
19	1.027	0.689	1.716	2.490	$0.634^{+2.779}_{-0.257}$	$\log g$	r_{012}	3p	x	x
20	0.894	0.528	1.723	3.721	$0.624^{+2.124}_{-0.247}$	$\log g$	r_{012}	5p	✓	✓
21	1.172	0.862	1.473	2.231	$0.597^{+2.734}_{-0.249}$	ρ	r_{012}	3p	x	x
22	0.874	0.776	1.480	3.462	$0.592^{+2.150}_{-0.244}$	ρ	r_{012}	5p	✓	✓
23	2.003	1.490	2.174	2.597	$0.631^{+2.548}_{-0.260}$	$\log g, L_{\text{Phot}}$	r_{012}	3p	x	x
24	1.938	1.501	2.181	3.829	$0.610^{+2.074}_{-0.239}$	$\log g, L_{\text{Phot}}$	r_{012}	5p	✓	✓
25	2.116	1.524	1.931	2.338	$0.579^{+2.169}_{-0.234}$	L_{Phot}, ρ	r_{012}	3p	x	x
26	2.036	1.532	1.938	3.570	$0.579^{+1.970}_{-0.232}$	L_{Phot}, ρ	r_{012}	5p	✓	✓
27	1.172	0.862	1.801	2.541	$0.597^{+2.734}_{-0.249}$	$\log g, \rho$	r_{012}	3p	x	x
28	0.874	0.776	1.808	3.772	$0.592^{+2.150}_{-0.244}$	$\log g, \rho$	r_{012}	5p	✓	✓
29	2.117	1.525	2.259	2.648	$0.579^{+2.169}_{-0.233}$	$\log g, L_{\text{Phot}}, \rho$	r_{012}	3p	x	x
30	2.036	1.533	2.266	3.879	$0.579^{+1.970}_{-0.232}$	$\log g, L_{\text{Phot}}, \rho$	r_{012}	5p	✓	✓
31	2.278	1.578	2.312	2.306	$0.677^{+5.342}_{-0.314}$	$\log g, L_{\text{Phot}}, \rho$	r_{02}		x	x
32	1.320	1.119	1.502	2.323	$0.631^{+3.962}_{-0.267}$	$\log g, L_{\text{Phot}}, \rho$	r_{02}		✓	✓
33	1.220	0.692			$0.633^{+3.119}_{-0.251}$	ϖ	r_{012}	3p	x	x
34	1.122	0.531			$0.612^{+2.182}_{-0.231}$	ϖ	r_{012}	5p	✓	✓

the inferred values. It should however still be noted that the models are obtained with parameters and physics outside our current understanding of appropriate values. The ratios can reliably determine that Kepler-444 does not have a convective core at its current age. However, models with induced early convective cores lead to drive the fit to older models, where the influence of the convective core has disappeared from the model, and due to the ratios providing the best constraint on the age of the star, this is not counteracted by other observables. The age of the model is however also dependent on the input physics and parameters, and this effect can therefore not be studied in detail here.

It is important to note that this trend is not observed when comparing \mathcal{M}_{12} and \mathcal{M}_{13} . Here, \mathcal{M}_{13} with a large τ_{core} has a lower inferred age than \mathcal{M}_{12} , while the difference in age is also lower than what is observed for the models in this work. Thus, this effect might be

mostly related to the way overshooting is prescribed in the models presented in this work. However, to definitively determine this, it would require a larger set of models using the same framework as B19 to compare to, and is thus not explored further in this work.

When comparing cases 17 through 24 to case 9 and 16, it becomes apparent that while ρ and $\log g$ increases the χ^2 of \mathcal{M}_{12} and \mathcal{M}_{13} almost equally, L_{Phot} increases the χ^2 of \mathcal{M}_{12} significantly more than for \mathcal{M}_{13} . This difference is larger than the discrepancy between the χ^2 of the models in case 31 where \mathcal{M}_{13} is preferred. The conclusion to favour \mathcal{M}_{13} over \mathcal{M}_{12} is thus in terms of classical parameters primarily driven by the fitted L_{Phot} value. Meanwhile, this does not increase the determined value of τ_{core} in the fits using BASTA, showing no correlation between this parameter and the convective core lifetime of the models in this work.

Finally, we also repeated the analysis outlined in this subsection

with each frequency ratio weighted as an individual measurement, as mentioned at the start of the section (i.e. setting N_i to 1 in Eq. (10) when computing χ_r^2). Across all cases, it leads to a large reduction in the number of models with high likelihoods, which causes the posteriors (Fig. 4) to become more jagged and multi-modal. However, the convective core size evolution of the highest likelihood tracks presented in Fig. 6 and the overall determined parameters does not change significantly. Specifically, τ_{core} changes to have a median value around 1 Gyr, with an upper bound around ~ 4.5 Gyr (compared with the ~ 0.6 Gyr and ~ 3.5 Gyr from fitting with N_i equal to the number of ratios), with the increase heavily driven by two tracks in the posterior with a large likelihood, that has high τ_{core} and ages. Specifically, these ages are ~ 13 Gyr, above the 84th percentile of the posterior, and close to the age of the Universe. The inferred larger upper bound using this unweighted scheme is therefore correlated with an increased inferred age.

In terms of the comparison between \mathcal{M}_{12} and \mathcal{M}_{13} when the frequency ratios are weighted as individual measurements, it shows a lower χ^2 for \mathcal{M}_{13} than \mathcal{M}_{12} in cases 5, 7 and 31. This change for case 5 and 7 is due to the deviation of T_{eff} for \mathcal{M}_{13} not dominating the χ^2 , as is the case when the ratio contribution is normalised. The conclusion of case 31 remains unchanged, as the χ^2 contribution of L_{phot} already compensated for the T_{eff} contribution.

From the discussion above, and the fits presented in Table 3, we can conclude that τ_{core} can be constrained to be lower than 4 Gyr as this is consistent with all fits apart from the r_{02} ratio fits. As mentioned, this is obtained using non-standard stellar models, where the expected value would be constrained to be within 1 Gyr.

6 CONCLUSIONS

In this work, we have studied the survival of the initial convective core of Kepler-444. In the work of [Buldgen et al. \(2019\)](#) it was determined to have an unusually long lifetime of the convective core (~ 7.85 Gyr) of the old ($\sim 11 \pm 1$ Gyr) sub-solar mass ($\sim 0.748 \pm 0.044 M_{\odot}$) star, i.e. an order of magnitude longer than what our current understanding of stellar evolution suggests. We produced a grid of stellar models with a high sampling of input parameters and artificially induced long convective-core lifetimes to determine the properties of Kepler-444 by fitting the observations to the grid using the BASTA code. The determined fundamental properties were consistent with previous studies, however we found a convective-core lifetime of $0.597^{+2.151}_{-0.244}$ Gyr by fitting the effective temperature, T_{eff} , metallicity, [Fe/H], mean density, ρ , and the r_{012} frequency separation ratio sequence to the grid.

While this lifetime is reasonably large, inspecting the highest-likelihood models in the grid reveals this to possibly not be due to a signature in the observed frequency ratios. Rather, the models with a high likelihood have no convective core signature left in the interior profile, where the models with a longer convective-core lifetime have evolved for longer before reaching this state. This indicates that the inclusion of an artificially induced longer convective-core lifetime introduces an age bias, systematically increasing the determined age of the star, when using the framework for stellar models applied in this study.

Additionally, we varied the sets of observations used when fitting to further study what can lead to the inference of long convective-core lifetimes. First, the choices related to how the mode frequency ratios are fitted to the best-fit models from [Buldgen et al. \(2019\)](#) were varied. The largest differences were seen when switching between including or excluding two potentially unreliable frequency

ratios flagged by [Davies et al. \(2016\)](#) (failing their quality check) from the fitted ratios. This is also in agreement with the possibility for high-frequency ratios being shifted to larger amplitudes due to surface magnetic activity, making them less reliable ([Thomas et al. 2021](#)). Large differences were also seen when including or excluding the covariances between the ratios in the computation of the error function. As the frequency ratios per construction repeatedly use the same frequency modes in their determination, they are inherently correlated and these correlations are important to consider. The conclusion to prefer a model with a long convective-core lifetime was only recovered when the two prior-dominated frequencies were included, when the covariance of the mode frequency ratios was not considered, or when only fitting the r_{02} frequency ratios.

Lastly, we repeated the fit for different sets of classical parameters to determine what observations drive the inference of a long convective-core lifetime and to verify the stability of the determined convective-core lifetime across the observed parameters. Only fits using the frequency ratio fit choices as mentioned above and including the luminosity derived by [Buldgen et al. \(2019\)](#) as a fitting parameter recovered the conclusion of preferring a long lifetime convective core. From the Bayesian marginalised posteriors determined from each fit, the median and 84th percentile were extracted with the median reliably around 0.6 Gyr, while the 84th percentile was reliably within ~ 3.5 Gyr. This large upper bound on convective core lifetime does however suggest that frequency ratios presumably only provide a weak constraint on this parameter.

This study exemplifies the difficulties of accurately inferring stellar interiors, both in the present and how it evolves. While the approach of varying the geometric cut-off g_{cut} in the overshoot description allowed for varied sizes and evolution of convective cores, there are no physical argument for changing its value from the solar-calibrated one. The change of inferred core evolution with inclusion or exclusion of the two frequency modes highlight the difficulties in determination of mode frequencies. While they can be determined to a high precision, the heavily prior-reliant methods for their determination can not always guarantee their accuracy. Also, if one does not consider the covariance of the mode frequency ratios it can easily lead to wrong conclusions as the differences in ratios between different models can be quite minute. Lastly, the appearance of an early convective core might not be well constrained by the frequency ratios and it in some cases simply leads to determination of older models where the influence of the early convective core had almost disappeared.

This is therefore not conclusive proof that Kepler-444 did not have a large convective core during its early evolution, but the most likely scenario is that it did not. Additionally, the non-zero determination could simply be the result of the convective-core lifetime producing older models as they take longer to reach an interior structure without signatures of a convective core. However, we can conclude that the model from [Buldgen et al. \(2019\)](#) without a long convective-core lifetime is preferred over their originally determined best fit model with a long convective-core lifetime within our choices of frequency ratios fitting. Our analysis reliably determines a short convective-core lifetime with determined stellar properties consistent with previous studies, and with standard stellar evolution theory.

ACKNOWLEDGEMENTS

The authors thank Dr. Gaël Buldgen for the cooperation during this work, for providing the data needed for the comparisons, and for the very helpful and detailed comments as referee of this work. The authors also thank Prof. Dr. Jørgen Christensen-Dalsgaard and

Prof. Dr. Achim Weiss for contributing their expertise on stellar evolution models for this work.

MLW acknowledges support from the Carlsberg Foundation (grant agreement CF19-0649). Funding for the Stellar Astrophysics Centre is provided by The Danish National Research Foundation (Grant agreement No. DNR106). AS acknowledges support from the European Research Council Consolidator Grant funding scheme (project ASTEROCHRONOMETRY, G.A. n. 772293, <http://www.asterochronometry.eu>). The numerical results presented in this work were obtained at the Centre for Scientific Computing, Aarhus <http://phys.au.dk/forskning/cscaa/>. This work has made use of data from the European Space Agency (ESA) mission *Gaia* (<https://www.cosmos.esa.int/gaia>), processed by the *Gaia* Data Processing and Analysis Consortium (DPAC, <https://www.cosmos.esa.int/web/gaia/dpac/consortium>). Funding for the DPAC has been provided by national institutions, in particular the institutions participating in the *Gaia* Multilateral Agreement.

DATA AVAILABILITY

The data and code for the data presented in this paper is available at <https://github.com/MLWinther/Kepler444>.

REFERENCES

- Adelberger E. G., et al., 2011, *Reviews of Modern Physics*, **83**, 195
- Aerts C., Christensen-Dalsgaard J., Kurtz D. W., 2010, *Asteroseismology*. Springer Science & Business Media
- Aguirre Børsen-Koch V., et al., 2022, *MNRAS*, **509**, 4344
- Akeson R. L., et al., 2013, *PASP*, **125**, 989
- Angulo C., et al., 1999, *Nuclear Phys. A*, **656**, 3
- Antonov I., Saleev V., 1980, *USSR Computational Mathematics and Mathematical Physics*, **19**, 252
- Asplund M., Grevesse N., Sauval A. J., Scott P., 2009, *ARA&A*, **47**, 481
- Baglin A., et al., 2006, in 36th COSPAR Scientific Assembly. p. 3749
- Ball W. H., Gizon L., 2014, *A&A*, **568**, A123
- Basu S., Chaplin W., 2017, *Asteroseismic Data Analysis: Foundations and Techniques*. Princeton Series in Modern Observational Astronomy, Princeton University Press, <https://books.google.dk/books?id=dQmTAQAACAAJ>
- Böhm-Vitense E., 1958, *Z. Astrophys.*, **46**, 108
- Borucki W. J., et al., 2010, *Science*, **327**, 977
- Bourrier V., et al., 2017, *A&A*, **602**, A106
- Bratley P., Fox B., 1988, *ACM Transactions on Mathematical Software*, **14**, 88
- Brown T. M., 1984, *Science*, **226**, 687
- Buldgen G., et al., 2019, *A&A*, **630**, A126
- Campante T. L., et al., 2015, *Astrophysical Journal*, **799**, 1
- Chaplin W. J., Miglio A., 2013, *ARA&A*, **51**, 353
- Christensen-Dalsgaard J., 2008, *Ap&SS*, **316**, 113
- Christensen-Dalsgaard J., Gough D., 1984, in Ulrich R. K., Harvey J., Rhodes E. J. J., Toomre J., eds, *Solar Seismology from Space*. pp 199–204
- Christensen-Dalsgaard J., Dappen W., Lebreton Y., 1988, *Nature*, **336**, 634
- Christensen-Dalsgaard J., Proffitt C. R., Thompson M. J., 1993, *ApJ*, **403**, L75
- Cunha M. S., et al., 2021, *Monthly Notices of the Royal Astronomical Society*, **508**, 5864–5885
- Daepfen W., Mihalas D., Hummer D. G., Mihalas B. W., 1988, *ApJ*, **332**, 261
- Davies G. R., Handberg R., Miglio A., Campante T. L., Chaplin W. J., Elsworth Y., 2014, *MNRAS*, **445**, L94
- Davies G. R., et al., 2016, *MNRAS*, **456**, 2183
- Deheuvels S., et al., 2010, *A&A*, **514**, A31
- Deheuvels S., Brandão I., Silva Aguirre V., Ballot J., Michel E., Cunha M. S., Lebreton Y., Appourchaux T., 2016, *A&A*, **589**, A93
- Dupuy T. J., Kratter K. M., Kraus A. L., Isaacson H., Mann A. W., Ireland M. J., Howard A. W., Huber D., 2016, *ApJ*, **817**, 80
- EGgen O. J., 1956, *AJ*, **61**, 462
- Ferguson J. W., Alexander D. R., Allard F., Barman T., Bodnarik J. G., Hauschildt P. H., Heffner-Wong A., Tamanai A., 2005, *ApJ*, **623**, 585
- Formicola A., et al., 2004, *Physics Letters B*, **591**, 61
- Fox B., 1986, *ACM Transactions on Mathematical Software*, **12**, 362
- Gaia Collaboration et al., 2016, *A&A*, **595**, A1
- Gaia Collaboration Vallenari A., et al. 2022, in preparation
- Hammer J., et al., 2005, *Nuclear Physics A*, **758**, 363
- Hidalgo S. L., et al., 2018, *The Astrophysical Journal*, **856**, 0
- Høg E., et al., 2000a, *A&A*, **355**, L27
- Høg E., et al., 2000b, *A&A*, **357**, 367
- Howell S. B., et al., 2014, *PASP*, **126**, 398
- Hummer D. G., Mihalas D., 1988, *ApJ*, **331**, 794
- Iglesias C. A., Rogers F. J., 1996, *ApJ*, **464**, 943
- Iliadis C., 2015, *Nuclear Physics of Stars*. Wiley, <https://books.google.dk/books?id=kLZNCAAQBAJ>
- Jakeš J., 1988, , doi:10.21136/AM.1988.104299
- Joe S., Kuo F., 2003, *ACM Transactions on Mathematical Software*, **29**, 49
- Jørgensen B. R., Lindegren L., 2005, *A&A*, **436**, 127
- Kippenhahn R., Weigert A., Weiss A., 2012, *Stellar Structure and Evolution*, second edition edn. Springer
- Kippenhahn R., Weigert A., 1990, *Stellar structure and evolution*. New York, NY (USA); Springer-Verlag New York Inc.
- Kjeldsen H., Bedding T. R., Christensen-Dalsgaard J., 2008, *ApJ*, **683**, L175
- Levenberg K., 1944, *Quarterly of Applied Mathematics*, **2**, 164
- Lindegren L., et al., 2021, *A&A*, **649**, A4
- Mack C. E., Strassmeier K. G., Ilyin I., Schuler S. C., Spada F., Barnes S. A., 2018, *A&A*, **612**, A46
- Mihalas D., Dappen W., Hummer D. G., 1988, *ApJ*, **331**, 815
- Mihalas D., Hummer D. G., Mihalas B. W., Daepfen W., 1990, *ApJ*, **350**, 300
- Nordlund Å., Stein R. F., Asplund M., 2009, *Living Reviews in Solar Physics*, **6**, 2
- Nordström B., et al., 2004, *A&A*, **418**, 989
- Pedersen M. G., Aerts C., Pápics P. I., Rogers T. M., 2018, *A&A*, **614**, A128
- Pezzotti C., Eggenberger P., Buldgen G., Meynet G., Bourrier V., Mordasini C., 2021, *A&A*, **650**, A108
- Rendle B. M., et al., 2019, *MNRAS*, **484**, 771
- Ricker G. R., et al., 2014, in *Space Telescopes and Instrumentation 2014: Optical, Infrared, and Millimeter Wave*. p. 914320 ([arXiv:1406.0151](https://arxiv.org/abs/1406.0151)), doi:10.1117/12.2063489
- Rogers F. J., Iglesias C. A., 1992, *ApJS*, **79**, 507
- Rogers F. J., Nayfonov A., 2002, *ApJ*, **576**, 1064
- Rogers F. J., Swenson F. J., Iglesias C. A., 1996, *ApJ*, **456**, 902
- Roman N. G., 1955, *ApJS*, **2**, 195
- Roxburgh I. W., 2009, *A&A*, **493**, 185
- Roxburgh I. W., 2018, arXiv e-prints, p. arXiv:1808.07556
- Roxburgh I. W., Vorontsov S. V., 2003, *A&A*, **411**, 215
- Roxburgh I. W., Vorontsov S. V., 2013, *A&A*, **560**, A2
- Sahlholdt C. L., Silva Aguirre V., Casagrande L., Mosumgaard J. R., Bojsen-Hansen M., 2018, *MNRAS*, **476**, 1931
- Salaris M., Cassisi S., 2017, *Royal Society Open Science*, **4**, 170192
- Salpeter E. E., 1955, *ApJ*, **121**, 161
- Scuflaire R., Théado S., Montalbán J., Miglio A., Bourge P. O., Godart M., Thoul A., Noels A., 2008a, *Ap&SS*, **316**, 83
- Scuflaire R., Montalbán J., Théado S., Bourge P. O., Miglio A., Godart M., Thoul A., Noels A., 2008b, *Ap&SS*, **316**, 149
- Silva Aguirre V., Ballot J., Serenelli A. M., Weiss A., 2011, *A&A*, **529**, A63
- Silva Aguirre V., et al., 2013, *ApJ*, **769**, 141
- Silva Aguirre V., et al., 2015, *MNRAS*, **452**, 2127
- Silva Aguirre V., et al., 2017, *ApJ*, **835**, 173
- Smitha H. N., Solanki S. K., 2017, *A&A*, **608**, A111
- Sobol I., 1977, *USSR Computational Mathematics and Mathematical Physics*, **16**, 236

Sobol I., Levithan Y., 1976, IPM Akademii Nauk SSSR
 Sono T., Samadi R., Belkacem K., Ludwig H. G., Caffau E., Mosser B., 2015, *A&A*, **583**, A112
 Stalport M., Matthews E. C., Bourrier V., Leleu A., Delisle J. B., Udry S., 2022, arXiv e-prints, p. arXiv:2209.06810
 Tenenbaum P., et al., 2013, *ApJS*, **206**, 5
 Thomas A. E. L., Chaplin W. J., Basu S., Rendle B., Davies G., Miglio A., 2021, *MNRAS*, **502**, 5808
 Thoul A. A., Bahcall J. N., Loeb A., 1994, *ApJ*, **421**, 828
 Trampedach R., 2010, *Ap&SS*, **328**, 213
 Verma K., Rørsted J. L., Serenelli A. M., Aguirre Børsen-Koch V., Winther M. L., Stokholm A., 2022, *MNRAS*, **515**, 1492
 Vogt S. S., et al., 1994, in Crawford D. L., Craine E. R., eds, Society of Photo-Optical Instrumentation Engineers (SPIE) Conference Series Vol. 2198, Instrumentation in Astronomy VIII. p. 362, doi:10.1117/12.176725
 Weiss A., Schlattl H., 2008, *Astrophysics and Space Science*, **316**, 99
 Wilson O. C., 1962, *ApJ*, **136**, 793
 Zhang Q.-S., Christensen-Dalsgaard J., Li Y., 2022, *MNRAS*, **512**, 4852
 van Leeuwen F., 2007, *A&A*, **474**, 653

APPENDIX A: EQUILIBRIUM OF ${}^3\text{He}$

The equilibrium mass fraction of ${}^3\text{He}$, $(X_{{}^3\text{He}})_e$, present in the core can be derived following Iliadis (2015). It is based on the reaction rates in the core and the presence of other materials, where the S -factors used for the reaction rates are those of Adelberger et al. (2011). This assumes an isolated system with no material entering from exterior sources. As the consumption rate of ${}^3\text{He}$ is larger than its creation rate in the PP-chains dominating the reactions in the core, there should be a low amount of ${}^3\text{He}$, only present in the delay between creation and consumption. The theoretical equilibrium amount can then be computed for the core evolution of a stellar model and compared to the actual amount present, to determine if any has been fed to the core through mixing with the surrounding material.

An example of this can be seen in Fig. A1, where the convective core mass fraction and central ${}^3\text{He}$ mass fraction evolution is shown for two GARSTEC models with the same input as \mathcal{M}_{13} , for two different values of overshooting efficiency. For $f_{\text{ove}} = 0$, and thereby no overshoot, the abundance of ${}^3\text{He}$ follows the computed equilibrium, while for $f_{\text{ove}} = 0.015$, it is clearly larger (≈ 1.8 times as much, slowly reducing) whereby it shows that overshooting indeed injects additional ${}^3\text{He}$ into the core. The abundance evolution is almost identical to those presented in Fig. 1 before an age of ~ 7.85 Gyr, whereby one can conclude that \mathcal{M}_{12} follows the equilibrium amount of ${}^3\text{He}$, while \mathcal{M}_{13} only does so towards the end of its evolution, after the convective core disappears.

APPENDIX B: ÉCHELLE OF BEST-FIT MODELS

While the frequency ratios of the HLM are shown in Fig. 5, it can also be informative to look at the échelle diagrams. The uncorrected frequencies are shown in Fig. B1, while a version with model frequencies corrected for the surface effect is shown in Fig. B2. Here the two term correction from Ball & Gizon (2014) were used with the fitted coefficients $a_{-1} = 7.308 \times 10^{-10}$ and $a_3 = -7.331 \times 10^{-9}$.

The large offset between modelled and observed frequencies in the uncorrected échelle diagram Fig. B1 indicates that the HLM is slightly too young.

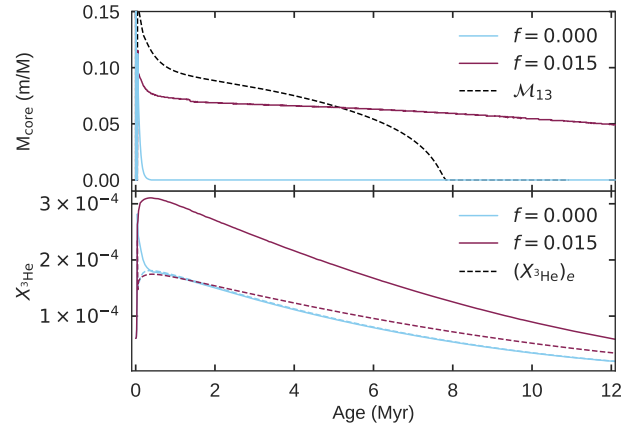


Figure A1. The evolution of the convective core size (*left*) and ${}^3\text{He}$ abundance (*right*) as a function of age, of two GARSTEC models of similar input to that of \mathcal{M}_{13} apart from overshooting. The model with a large overshooting efficiency clearly shows an increased abundance of ${}^3\text{He}$ compared to the model without overshooting, which is also a large increase compared to the equilibrium amount.

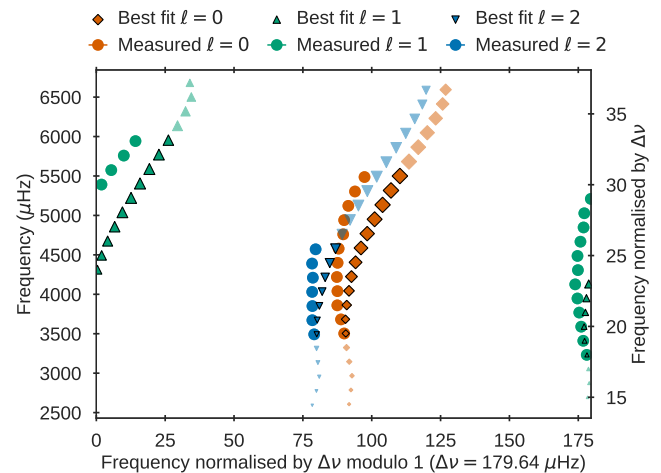


Figure B1. Échelle diagram of the observed frequencies and the uncorrected model frequencies of the HLM. The two prior dominated frequencies ν ($\ell = 2$, $n = 24, 25$) have been omitted.

APPENDIX C: GRID RESOLUTION

The parameters for each track in the grid described in Section 3.3 are drawn from continuous distributions, using the (quasi-)random Sobol-sequence (Sobol & Levithan 1976; Sobol 1977; Joe & Kuo 2003; Fox 1986; Bratley & Fox 1988; Antonov & Saleev 1980), as described in Section 3. This ensures an uniform sampling of the parameter space, and avoids clumpy over-densities in the parameter space that is usually encountered for Cartesian or pseudo-random methods (Aguirre Børsen-Koch et al. 2022). Only two parameters are discretised, initial mass as the starting models have only been prepared in steps of $0.001 M_{\odot}$, and alpha-element enhancement as opacity tables have only been computed in steps of 0.1 dex.

Due to the grid being constructed this way, it does not have a regular measure of resolution in each parameter, as is e.g. the case

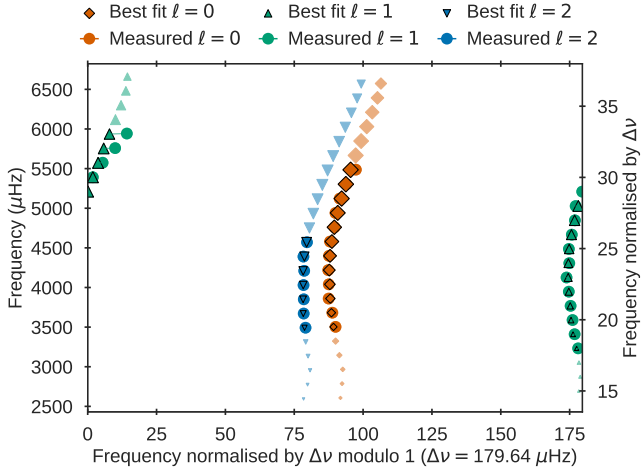


Figure B2. Échelle diagram of the observed frequencies and the model frequencies of the HLM corrected using the combined correction of [Ball & Gizon \(2014\)](#). The two prior dominated frequencies ν ($\ell = 2$, $n = 24, 25$) have been omitted.

for Cartesian-sampled grids with a fixed sampling in each parameter. To represent the resolution of the grid, the initial parameters of the track that constitute the grid are instead shown in [Fig. C1](#) for each combination of parameters. This shows a high sampling of each combination of parameters, while some slight repetition of patterns within these also shows the sampling to not be completely random.

This paper has been typeset from a $\text{\TeX}/\text{\LaTeX}$ file prepared by the author.

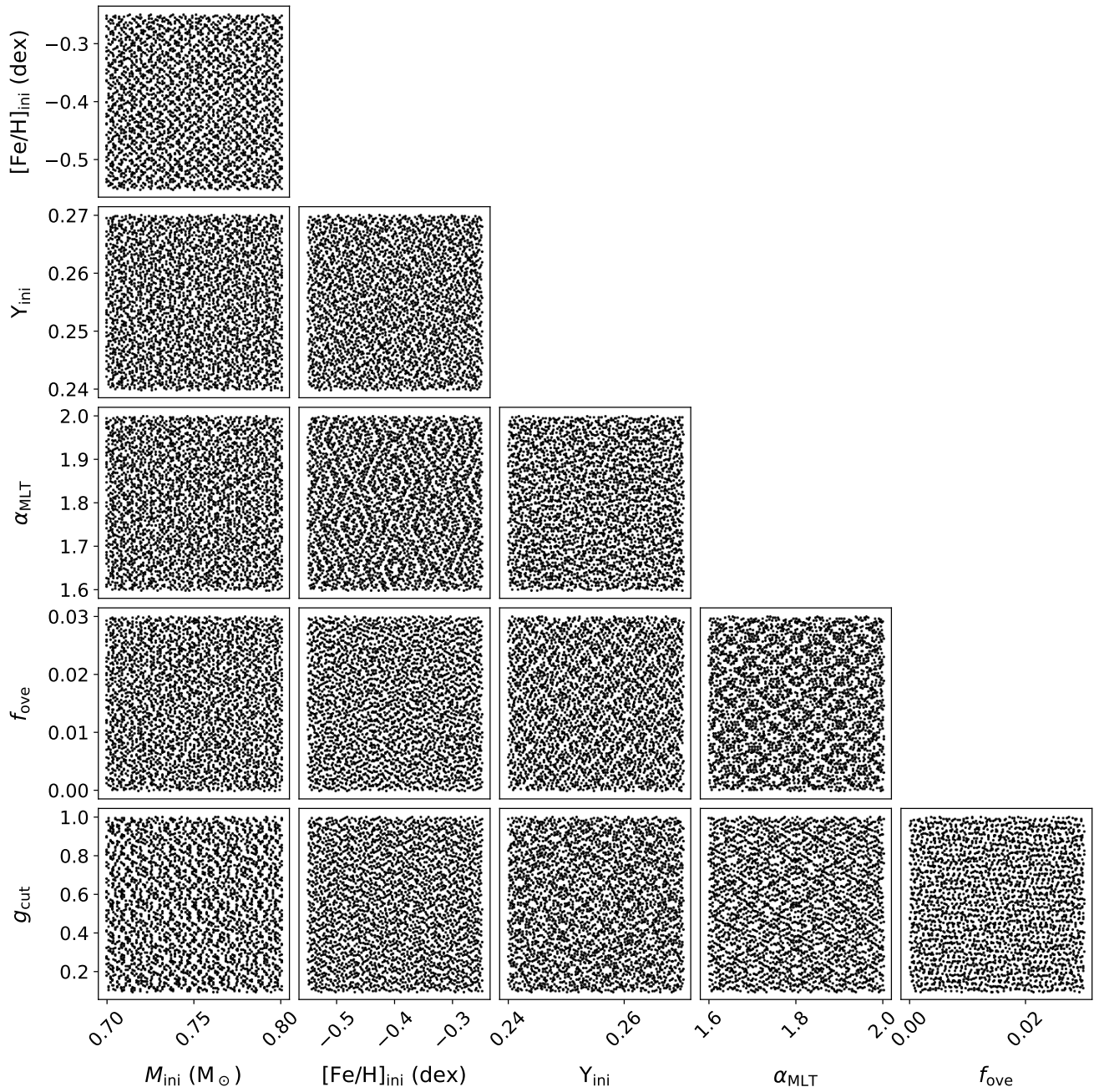


Figure C1. Distribution of initial parameters of tracks in the grid. $[\alpha/\text{Fe}]$ is not shown, as it can only be one of two discrete values.